

Spatiotemporal Properties of Compressible Magnetohydrodynamic Turbulence from Space Plasma

Siqi Zhao,¹ Huirong Yan,^{1,2,*} Terry Z. Liu,^{3,†} Chuanpeng Hou,¹ and Ka Ho Yuen⁴

¹*Institut für Physik und Astronomie, Universität Potsdam, D-14476 Potsdam, Germany*

²*Deutsches Elektronen Synchrotron (DESY), Platanenallee 6, D-15738 Zeuthen, Germany*

³*Shandong Key Laboratory of Space Environment and Exploration Technology, Institute of Space Sciences, School of Space Science and Technology, Shandong University, Shandong, China.*

⁴*Institute of Science and Technology for Deep Space Exploration, Nanjing University, P.R. China*

(Dated: March 10, 2026)

Previous studies have established that a weak-to-strong transition occurs in Alfvénic magnetohydrodynamic (MHD) turbulence as energy cascades from large to small scales. However, the spatiotemporal (frequency–wavenumber) properties of compressible MHD turbulence involving all eigenmodes, which encode the strength of nonlinear interactions, remain difficult to characterize observationally. Consequently, whether a similar weak-to-strong transition occurs in compressible turbulence remains elusive. Using a novel multi-spacecraft, polarization-based mode-decomposition technique with measurements from the Cluster spacecraft in Earth’s magnetosheath, we obtain spatiotemporal power spectra of all MHD eigenmodes and present the first quantitative assessment of nonlinear frequency broadening. Our results show that slow modes exhibit a weak-to-strong transition, evolving from wave-like peaks to frequency-broadened spectra as nonlinearity increases, whereas fast modes remain weakly turbulent with narrow peaks near their eigenfrequencies. Both Alfvénic and compressible fluctuations contribute significantly to low-frequency, large-scale quasi-two-dimensional structures. These findings provide a comprehensive observational characterization of compressible turbulence across mode composition, spatiotemporal scales, and weak/strong turbulence regimes, with implications for energetic particle transport, turbulent dynamos, plasma heating, and solar wind–magnetosphere coupling.

I. INTRODUCTION

Plasma turbulence is ubiquitous and plays a fundamental role in astrophysical and space plasmas, spanning environments from galaxy clusters and the interstellar medium to accretion disks and the heliosphere [1–7]. Turbulent processes transfer energy across a wide range of spatial and temporal scales, typically characterized by broadband spectra in both frequency and wavenumber space [8, 9]. Previous simulations [10–12] and observations [13] have demonstrated a weak-to-strong transition in incompressible Alfvénic turbulence as energy cascades from large to small scales. However, the spatiotemporal (frequency–wavenumber) properties of compressible MHD turbulence involving all eigenmodes, which encode the strength of nonlinear interactions, remain difficult to characterize observationally. Consequently, whether a similar weak-to-strong transition occurs in compressible turbulence remains elusive. Understanding this self-organized process is essential for elucidating the physics of energy cascades in compressible MHD turbulence.

In a homogeneous plasma with a uniform background magnetic field \mathbf{B}_0 , small-amplitude fluctuations, where linear terms ($\delta V_{\text{rms}} V_A$, $\delta B_{\text{rms}} B_0$) dominate over nonlinear terms (δV_{rms}^2 , δB_{rms}^2), can be decomposed into three linear MHD eigenmodes: the incompressible Alfvén mode, and the compressible fast and slow modes [14, 15].

Here, V_A is the Alfvén speed, and δV_{rms} and δB_{rms} are the root-mean-square (rms) of proton velocity and magnetic field fluctuations, respectively. For each mode, the temporal power spectrum at a given wavevector \mathbf{k} peaks at its eigenfrequency ω_{wave} . In the linear regime, this peak reduces to a δ -function at ω_{wave} , satisfying the corresponding dispersion relations [14].

In turbulent plasmas, fluctuations are not expected to strictly satisfy linear MHD dispersion relations. In the temporal power spectrum, the idealized δ -function signature of the linear MHD eigenmodes is replaced by a finite-width feature due to nonlinear interactions [13, 16]. In MHD theory, turbulence is classified into weak and strong regimes based on the strength of nonlinear coupling [11, 13, 17]. In the weak-turbulence regime, interactions among counter-propagating wave packets are sufficiently weak that fluctuations remain predominantly wave-like [18]. In contrast, in the strong-turbulence regime, fluctuations undergo strong nonlinear interactions and reach a critical balance between the linear wave time $\tau_{\text{wave}} = 1/\omega_{\text{wave}}$ and the nonlinear time $\tau_{\text{nl}} = 1/\omega_{\text{nl}}$, where ω_{nl} is the nonlinear frequency [19, 20]. In this regime, off-dispersion fluctuations are expected to dominate the spectrum [11, 13], accounting for approximately 75%–80% of the total power [21]. Furthermore, theory predicts mode-dependent asymmetric frequency broadening [16]: (i) Alfvén and slow fluctuations develop a pronounced low-frequency continuum dominated by sufficiently small k_{\parallel} , while retaining spectral peaks near ω_{wave} at finite k_{\parallel} , where k_{\parallel} denotes wavenumbers parallel to \mathbf{B}_0 . (ii) In contrast, fast modes remain pre-

* huirong.yan@desy.de

† terryliuzixu@sdu.edu.cn

dominantly wave-like, exhibiting only modest nonlinear frequency broadening and contributing little power to the low-frequency continuum; accordingly, they exhibit comparatively weak nonlinearity across the inertial range [16, 22, 23].

Beyond mode-dependent nonlinear frequency broadening, mode-dependent cascade behaviors in wavenumber space further shape the spatiotemporal properties of compressible MHD turbulence. In the weak-turbulence regime, Alfvén modes transfer energy exclusively toward higher perpendicular wavenumbers k_{\perp} through resonant three-wave interactions [18], where k_{\perp} denotes the wavenumber perpendicular to \mathbf{B}_0 . In the strong-turbulence regime, Alfvén modes satisfy the critical-balance condition ($\tau_{\text{wave}} \sim \tau_{\text{nl}}$), leading to a scale-dependent anisotropic cascade characterized by $k_{\parallel} \propto k_{\perp}^{2/3}$ [20]. A comprehensive theoretical framework for compressible MHD turbulence that self-consistently incorporates slow and fast modes remains incomplete. Nevertheless, theoretical and numerical studies suggest that slow modes are passively cascaded by Alfvénic turbulence and exhibit similar anisotropic scalings [12, 24–26]. In contrast, fast modes are predicted to remain nearly isotropic, exhibiting an energy spectrum $E(k) \propto k^{-3/2}$ and being modulated by collisionless transit-time damping (TTD) which increases with obliquity at small scales [27–29], where $k = |\mathbf{k}|$. Despite substantial theoretical and numerical advances, direct observational characterizations of these mode-resolved spatiotemporal properties across both weak- and strong-turbulence regimes remain limited.

A reliable mode decomposition is a prerequisite for investigating the mode-resolved spatiotemporal properties of compressible MHD turbulence. Glassmeier et al. [30] decomposed the time series of fluctuations into three sets of forward and backward propagating MHD eigenmodes in frequency space. Cho et al. [25, 31] performed mode-decomposition in wavenumber space by projecting turbulent fluctuations onto the displacement vectors of the MHD eigenmodes. Zank et al. [32] proposed a linear mode-decomposition framework that, in addition to the ideal MHD eigenmodes, explicitly incorporates non-propagating entropy modes and magnetic-island (flux-rope) modes. All of these approaches rely fundamentally and entirely on linear MHD dispersion relations. However, as emphasized above, nonlinear interactions and the resulting frequency broadening drive turbulent fluctuations away from linear MHD dispersion relations [13, 16]. Such intrinsic departures may significantly limit the applicability of linear-based decomposition methods, particularly in the strong-turbulence regime. To address this limitation, Zhao et al. [33] recently introduced a polarization-based mode-decomposition method that separates Alfvénic and compressible fluctuations without explicitly enforcing linear dispersion relations. Nevertheless, their study does not further distinguish between fast and slow modes.

In this study, we further advance the polarization-

based mode-decomposition method of Zhao et al. [33], augmented by incorporating the phase correlation between fluctuations in magnetic field strength $\delta|\tilde{\mathbf{B}}|$ and plasma density $\delta\tilde{N}$. This methodological innovation enables a complete separation of Alfvén, slow, and fast contributions and allows direct estimation of the four-dimensional (4D) spatiotemporal power spectra without invoking spatiotemporal assumptions such as the Taylor hypothesis [34]. Using this approach and joint observations from the four Cluster spacecraft, we provide the first quantitative assessment of how the frequency broadening of three MHD eigenmodes depends on nonlinear interactions, enabling a direct test of whether a weak-to-strong transition occurs in the compressible regime.

II. METHODOLOGY

A. Data

The magnetic field data are obtained from the Fluxgate Magnetometer (FGM) [35] on the four Cluster spacecraft at a sampling rate of 22.5 Hz, selecting intervals with a high tetrahedron quality factor (TQF). Proton plasma parameters are obtained from the Cluster Ion Spectrometry’s Hot Ion Analyzer (CIS-HIA) [36] with a cadence of 4 s. Electron density data are obtained from the Plasma Electron And Current Experiment (PEACE) [37] on Cluster-2 and from the Waves of High frequency and Sounder for Probing of Electron density by Relaxation (WHISPER) [38] on Cluster-1, both with a cadence of 4 s. For the calculation of spatiotemporal power spectra, all magnetic field and plasma parameters are interpolated to a uniform resolution of 1 sample/s.

B. Basic MHD Theory

In turbulent plasma, MHD fluctuations consist of incompressible Alfvén modes, compressible fast and slow (magnetosonic) modes, as well as fluctuations that deviate from the MHD linear dispersion relations owing to nonlinear interactions [13, 16]. The linear dispersion relations of Alfvén, fast, and slow modes are given by [14]

$$f_{\text{A}} = k_{\parallel} V_{\text{A}} / (2\pi), \quad (1)$$

$$f_{\text{fast}} = k V_{\text{ph},+} / (2\pi), \quad (2)$$

$$f_{\text{slow}} = k V_{\text{ph},-} / (2\pi), \quad (3)$$

where f_{A} , f_{fast} , and f_{slow} denote the eigenfrequencies of Alfvén, fast, and slow modes, respectively. The phase speeds of fast and slow modes are given by

$$V_{\text{ph},\pm}^2 = \frac{1}{2} \{ (V_{\text{S}}^2 + V_{\text{A}}^2) \pm [(V_{\text{S}}^2 + V_{\text{A}}^2)^2 - 4V_{\text{S}}^2 V_{\text{A}}^2 \cos^2 \theta]^{\frac{1}{2}} \}, \quad (4)$$

where the ‘+’ and ‘−’ signs correspond to the fast and slow modes, respectively; V_{S} is the sound speed, and θ is the angle between \mathbf{k} and \mathbf{B}_0 .

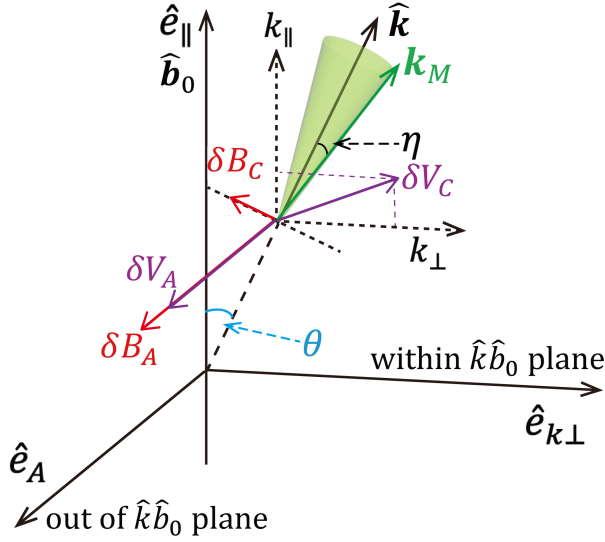


FIG. 1. Fluctuations in the $\hat{k}\hat{b}_0$ coordinates. Alfvénic magnetic and velocity fluctuations (δB_A and δV_A) are polarized perpendicular to the $\hat{k}\hat{b}_0$ plane, whereas compressible fluctuations (δB_C and δV_C) are polarized within the $\hat{k}\hat{b}_0$ plane. θ is the angle between $\hat{\mathbf{k}}$ and $\hat{\mathbf{b}}_0$, and η is the angle between timing-derived \mathbf{k}_M and SVD-derived $\hat{\mathbf{k}}$.

C. Mode-Decomposition Method

We decompose small-amplitude fluctuations into Alfvénic and compressible modes based on their polarization properties, following the method of Zhao et al. [33]. For compressible modes, oblique MHD fast (slow) modes are characterized by a positive (negative) phase correlation between fluctuations in magnetic field strength $\delta|\tilde{\mathbf{B}}|$ and density $\delta\tilde{N}$ [14, 15]. Furthermore, fast modes remain predominantly wave-like with weak nonlinear broadening across the entire inertial range, whereas slow modes increasingly deviate from their linear dispersion relations as nonlinearity increases [16]. Motivated by these properties, we further isolate fast modes from the compressible fluctuations by integrating the power within a $\pm 30\%$ frequency band centered at f_{fast} , taking into account the positive phase correlation between $\delta|\tilde{\mathbf{B}}|$ and $\delta\tilde{N}$. The remaining compressible fluctuations are likely dominated by a mixture of slow modes and positively phase-correlated magnetic-density fluctuations that deviate from the fast-mode dispersion relation.

As illustrated in Fig. 1, we analyze small-amplitude fluctuations in the $\hat{k}\hat{b}_0$ coordinates defined by the unit wavevector $\hat{\mathbf{k}}$ and unit background magnetic field $\hat{\mathbf{b}}_0 = \mathbf{B}_0/|\mathbf{B}_0|$ [13, 25, 39]. The associated orthonormal basis vectors are $\hat{\mathbf{e}}_{\parallel} = \hat{\mathbf{b}}_0$, $\hat{\mathbf{e}}_{k\perp} = \hat{\mathbf{b}}_0 \times (\hat{\mathbf{k}} \times \hat{\mathbf{b}}_0)/|\hat{\mathbf{b}}_0 \times (\hat{\mathbf{k}} \times \hat{\mathbf{b}}_0)|$, and $\hat{\mathbf{e}}_A = \hat{\mathbf{e}}_{k\perp} \times \hat{\mathbf{e}}_{\parallel}$. The unit wavevector $\hat{\mathbf{k}}(t, f_{\text{sc}})$ is determined using the singular value decomposition (SVD) based on the linearized Gauss's law for magnetism [40], where t is time, and f_{sc} is the spacecraft-frame frequency. Because turbulent eddies interact with the local rather

than the global magnetic field [41–43], we define the local mean magnetic field as $\mathbf{B}_0 = (\mathbf{B}(t - \tau/2) + \mathbf{B}(t + \tau/2))/2$, where $\tau = 1/f_{\text{sc}}$ is the timescale. The detailed procedure for constructing the spatiotemporal power spectra is described below.

First, the time series of fluctuations are transformed using the Morlet-wavelet transform [44], yielding Fourier-space fluctuations in geocentric-solar-ecliptic (GSE) coordinates: $\delta\tilde{\mathbf{B}}(t, f_{\text{sc}}) = [\delta\tilde{B}_X, \delta\tilde{B}_Y, \delta\tilde{B}_Z]$, $\delta\tilde{\mathbf{V}}_p(t, f_{\text{sc}}) = [\delta\tilde{V}_{pX}, \delta\tilde{V}_{pY}, \delta\tilde{V}_{pZ}]$, $\delta\tilde{N}_p(t, f_{\text{sc}})$, and $\delta\tilde{N}_e(t, f_{\text{sc}})$. The whole time interval is segmented into overlapping windows of $t_{\text{win}} = 5$ hours with a 30-minute shift to ensure adequate statistical sampling, where t_{win} is the window duration. To reduce edge effects from finite time series, each wavelet transform is performed over a $2t_{\text{win}}$ interval, with only the central t_{win} retained for analysis.

Second, based on MHD theory, Alfvénic velocity fluctuations $\delta\tilde{\mathbf{V}}_A$ are identified by their incompressibility, $\hat{\mathbf{k}} \cdot \delta\tilde{\mathbf{V}}_A = 0$, and perpendicularity to the local mean magnetic field, $\mathbf{B}_0 \cdot \delta\tilde{\mathbf{V}}_A = 0$. In contrast, compressible velocity fluctuations $\delta\tilde{\mathbf{V}}_C$ lie in the $\hat{k}\hat{b}_0$ plane and include contributions from fast and slow modes. Based on the linearized induction equation, Alfvénic magnetic fluctuations $\delta\tilde{\mathbf{B}}_A$ are polarized along $\hat{\mathbf{e}}_A$ and are given by $\delta\tilde{\mathbf{B}}_A = \delta\tilde{\mathbf{B}} \cdot \hat{\mathbf{e}}_A$, whereas compressible magnetic fluctuations $\delta\tilde{\mathbf{B}}_C$ lie within the $\hat{k}\hat{b}_0$ plane and are polarized along $\hat{\mathbf{e}}_C = \hat{\mathbf{e}}_A \times \hat{\mathbf{k}}$, i.e., $\delta\tilde{\mathbf{B}}_C = \delta\tilde{\mathbf{B}} \cdot \hat{\mathbf{e}}_C$ (Fig. 1). Proton and electron density fluctuations ($\delta\tilde{N}_p$ and $\delta\tilde{N}_e$) arise entirely from compressible modes. The associated velocity, magnetic, and density powers are calculated as

$$P_{KA}(t, f_{\text{sc}}) = \delta\tilde{V}_A \delta\tilde{V}_A^*, \quad (5)$$

$$P_{KC}(t, f_{\text{sc}}) = \delta\tilde{V}_C \delta\tilde{V}_C^* = \delta\tilde{V}_{\parallel} \delta\tilde{V}_{\parallel}^* + \delta\tilde{V}_{k\perp} \delta\tilde{V}_{k\perp}^*, \quad (6)$$

$$P_{BA}(t, f_{\text{sc}}) = \delta\tilde{B}_A \delta\tilde{B}_A^*, \quad (7)$$

$$P_{BC}(t, f_{\text{sc}}) = \delta\tilde{B}_C \delta\tilde{B}_C^*, \quad (8)$$

$$P_{N_p}(t, f_{\text{sc}}) = \delta\tilde{N}_p \delta\tilde{N}_p^*, \quad (9)$$

$$P_{N_e}(t, f_{\text{sc}}) = \delta\tilde{N}_e \delta\tilde{N}_e^*. \quad (10)$$

where $\delta\tilde{V}_{\parallel}$ and $\delta\tilde{V}_{k\perp}$ are proton velocity fluctuations along $\hat{\mathbf{e}}_{\parallel}$ and $\hat{\mathbf{e}}_{k\perp}$, respectively.

Third, we determine wavevectors using multi-spacecraft timing analysis [45] for intervals with a tetrahedron quality factor $\text{TQF} > 0.8$, ensuring reliable and accurate wavenumber estimation (see Zhao et al. [39] for details). Unlike the SVD technique, which provides only a wavevector direction $\hat{\mathbf{k}}$ corresponding to the normal of the composite $\delta\tilde{\mathbf{B}}$ plane formed by superposed modes, the timing analysis yields the full wavevector \mathbf{k}_M from the inter-spacecraft phase differences of $\delta\tilde{\mathbf{B}}_M$, where $M = A$ and $M = C$ denote Alfvénic and compressible fluctuations, respectively. Because modes with distinct dispersion relations and wavevectors can coexist at the same frequency, \mathbf{k}_M (\mathbf{k}_A or \mathbf{k}_C) is not necessarily aligned with the SVD-derived $\hat{\mathbf{k}}$. We therefore regard the timing analysis results as reliable only when \mathbf{k}_M is closely aligned

with $\hat{\mathbf{k}}$, and restrict our analysis to cases where the angle η between them is below a prescribed threshold (Fig. 1).

Fourth, the power spectra are transformed into the rest frame of plasma flow by correcting the Doppler shift, $f_{\text{rest}} = f_{\text{sc}} - \mathbf{k}_M \cdot \mathbf{V}_p / (2\pi)$, where \mathbf{V}_p is the proton bulk velocity with the spacecraft velocity being negligible, and f_{rest} is the frequency in the rest frame of plasma flow. We adopt an absolute-frequency representation,

$$(f_{\text{rest}}, \mathbf{k}_M) = \begin{cases} (f_{\text{rest}}, \mathbf{k}_M) & \text{if } f_{\text{rest}} > 0, \\ (-f_{\text{rest}}, -\mathbf{k}_M) & \text{if } f_{\text{rest}} < 0, \end{cases} \quad (11)$$

which ensures positive frequencies by simultaneously reversing the signs of both frequency and wavevector when $f_{\text{rest}} < 0$.

Finally, we construct a set of $N_f \times N_{k_{\parallel}} \times N_{k_{\perp}}$ bins to obtain spatiotemporal power spectra of velocity, magnetic, and density fluctuations in the plasma flow frame. Each bin subtends approximately constant f_{rest} , k_{\parallel} , and k_{\perp} , with widths df_{rest} , dk_{\parallel} , and dk_{\perp} . The wavenumbers are calculated as $k = |\mathbf{k}_M|$, $k_{\parallel} = \mathbf{k}_M \cdot \hat{\mathbf{b}}_0$, and $k_{\perp} = \sqrt{\mathbf{k}_M^2 - k_{\parallel}^2}$. To focus on inertia-range MHD fluctuations, we restrict the analysis to $4/t_{\text{win}} < f_{\text{rest}} < f_{\text{cp}}/2$ Hz and $1/(100d_{\text{sc}}) < k < \min(1/\max(d_p, r_{\text{cp}}), \pi/d_{\text{sc}})$. Here, f_{cp} is proton gyrofrequency, d_{sc} is the spacecraft separation, d_p is the proton inertial length, r_{cp} is the proton gyroradius, and max and min denote the maximum and minimum. These bounds ensure adequate averaging over multiple wave periods and account for the intrinsic limitation of multi-spacecraft techniques, which are sensitive to spatial scales comparable to the spacecraft separation [45].

III. RESULTS

A. Overview

During 23:00-10:00 UT on 2-3 December 2003, the four Cluster spacecraft traversed the flank of Earth's magnetosheath in a tetrahedral configuration with $\text{TFQ} = 0.97$ and $d_{\text{sc}} = 200$ km. Fig. 2 presents an overview of the fluctuations measured by Cluster-1 in GSE coordinates. This interval has been used to investigate the transition from weak- to strong-turbulence regimes in Alfvénic turbulence [13] and the modulation of collisionless transit-time damping on compressible turbulence [39]. Here, we extend these studies by examining the spatiotemporal properties of compressible MHD turbulence and quantitatively assessing nonlinear frequency broadening.

Figs. 2(a-d) show that the magnetic field and plasma parameters remain relatively stable and homogeneous throughout the interval, a conclusion further supported by the time-correlation functions [13]. Fig. 2(e) shows that the average proton β_p is around 1.4. Fig. 2(h) shows that $\delta V_{\text{rms}}/V_A < 1$ and $\delta B_{\text{rms}}/B_0 \lesssim 1$, confirming that the small-amplitude condition is satisfied.

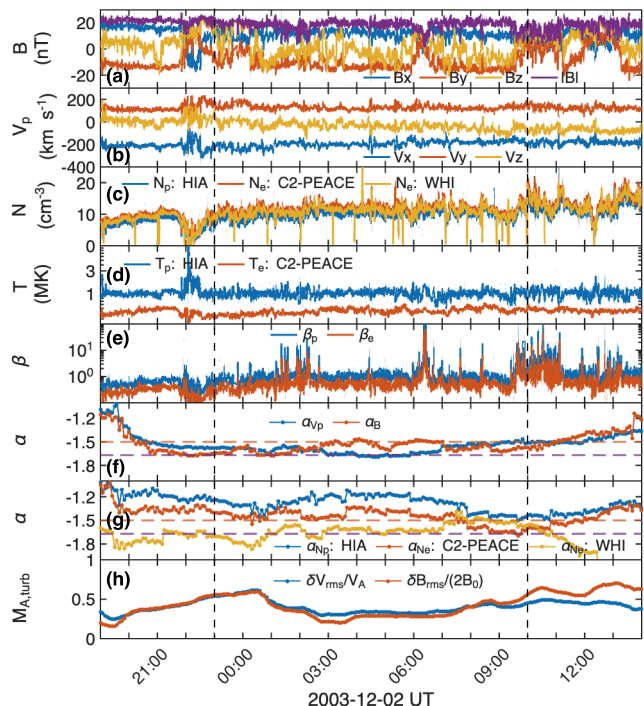


FIG. 2. Overview of fluctuations in Earth's magnetosheath. (a) Magnetic field. (b) Proton bulk velocity. (c) Proton density from CIS-HIA and electron density from PEACE and WHISPER. (d) Temperature. (e) Plasma β (the ratio of thermal to magnetic pressures). (f) Spectral slopes (α) of trace velocity and magnetic power spectra. (g) Spectral slopes (α) of density power spectra. (f,g) The horizontal dashed lines indicate $\alpha = -5/3$ and $-3/2$. (h) Turbulent Alfvén Mach number ($\delta V_{\text{rms}}/V_A$) and half of the relative amplitudes of the magnetic field ($\delta B_{\text{rms}}/(2B_0)$). Unless otherwise noted, all observations are from Cluster-1. The analysis is restricted to the interval between the two vertical dashed lines.

The entire interval is divided into overlapping 5-hour windows with a 5-minute step. For each window, we apply a fast Fourier transform (FFT) with five-point smoothing to obtain the trace power spectra of velocity, magnetic field, and density fluctuations. The spectral slopes are fitted in the spacecraft-frame frequency range $f_{\text{sc}} = [0.005f_{\text{cp}}, 0.1f_{\text{cp}}]$, where the average proton gyrofrequency is $f_{\text{cp}} = 0.24$ Hz. Fig. 2(f) shows that the velocity and magnetic spectra exhibit slopes between $-5/3$ and $-3/2$, indicating a well-developed turbulent state. Despite inconsistencies between proton and electron density measurements due to instrumental uncertainties (Fig. 2(c)), the density spectra remain stable (Fig. 3(g)), confirming the presence of compressible turbulence. Both PEACE and WHISPER electron density spectra exhibit slopes close to $-3/2$, approximately consistent with developed density fluctuations. Overall, these stable spectral characteristics demonstrate that this interval provides a suitable plasma environment for investigating the spatiotemporal properties of compressible MHD turbulence in a developed turbulent state.

B. Spatiotemporal power spectra of magnetic fluctuations

Using the mode-decomposition method described in Section II C, we obtain the spatiotemporal power spectra of this in situ turbulence interval in the plasma flow frame (Fig. 3). Since the magnetic, velocity, and density spectra exhibit similar spatiotemporal characteristics, we present the magnetic spectra in the main text, which are the most robust owing to their higher temporal resolution. The corresponding velocity and density spectra, together with additional magnetic results, are provided in Fig. 8 in Appendix A.

1. Alfvén modes

Fig. 3(a) shows that the $f_{\text{rest}} - k_{\perp}$ distribution of Alfvénic magnetic power, $P_{\text{BA}}(f_{\text{rest}}, k_{\perp}) = \int P_{\text{BA}}(f_{\text{rest}}, k_{\parallel}, k_{\perp}) dk_{\parallel}$, agrees well with the scaling $f_{\text{rest}} \propto k_{\perp}^{2/3}$. Since $f_{\text{rest}} \propto k_{\parallel}$ for Alfvén modes, this directly implies the anisotropic scaling $k_{\parallel} \propto k_{\perp}^{2/3}$. This relation is consistent with the critical-balance scaling for strong Alfvénic turbulence [20] and independently confirmed in Fig. 2 of [13].

Fig. 3(e) shows the $f_{\text{rest}} - k_{\parallel}$ distribution of Alfvénic magnetic power, $P_{\text{BA}}(f_{\text{rest}}, k_{\parallel}) = \int P_{\text{BA}}(f_{\text{rest}}, k_{\parallel}, k_{\perp}) dk_{\perp}$. For large scales ($k_{\parallel} < 10^{-5} \text{ km}^{-1}$), P_{BA} exhibits a nearly constant low-frequency component at $f_{\text{rest}} \sim 5 \times 10^{-4} \text{ Hz}$, as indicated by the nearly constant power-weighted mean frequency f_{P_m} and its $\pm\sigma$ bounds (white curves). The weak dependence of f_{P_m} on k_{\parallel} , together with the decrease of P_{BA} with increasing k_{\perp} (Fig. 4(a)), indicates that the dynamics of these Alfvénic fluctuations are predominantly governed by perpendicular scales, demonstrating that these fluctuations with $k_{\parallel} \ll k_{\perp}$ correspond to quasi-two-dimensional (quasi-2D) magnetic structures. The compressible magnetic power exhibits similar behavior (Fig. 8(g) in Appendix A), indicating that compressible fluctuations also contribute significantly to low-frequency, large-scale quasi-2D magnetic structures. The low-frequency behavior is consistent with the findings of simulations [16], which corresponds to the nonlinearity parameter $\chi \gg 1$ case since $\omega_{\text{wave}} = 0$. Such features are observed for both Alfvén and slow modes [16].

For $k_{\parallel} > 10^{-5} \text{ km}^{-1}$, f_{P_m} of Alfvénic magnetic power remains close to the Alfvén frequency f_A (pink dotted line in Fig. 3(e)), demonstrating nonlinear frequency broadening centered at f_A . In contrast, f_{P_m} of compressible magnetic power deviates significantly from the slow-mode frequency f_{slow} and is preferentially concentrated at frequencies lower than f_{slow} , especially at $k_{\parallel} > 7 \times 10^{-5} \text{ km}^{-1}$ (Figs. 8(f-h) in Appendix A). This behavior is likely attributable to the stronger nonlinearity of slow modes, for which numerical simulations predict enhanced low-

frequency power [16]. A quantitative characterization of nonlinear frequency broadening is presented in Section III C.

2. Compressible modes

Fig. 3(b) shows that the $f_{\text{rest}} - k_{\perp}$ distribution of compressible magnetic power, $P_{\text{BC}}(f_{\text{rest}}, k_{\perp}) = \int P_{\text{BC}}(f_{\text{rest}}, k_{\parallel}, k_{\perp}) dk_{\parallel}$, exhibits two distinct components. (1) One follows the fast-mode dispersion relations (black dotted line). (2) The other is concentrated at low frequencies and is approximately consistent with the scaling $f_{\text{rest}} \propto k_{\perp}^{2/3}$, similar to that found in P_{BA} (Fig. 3(a)).

As a preliminary diagnostic of compressible mode composition, we examine the phase correlation between fluctuations in magnetic field strength ($\delta|\mathbf{B}|$) and PEACE electron density ($\delta\tilde{N}_e$). Fig. 3(f) shows that in-phase fluctuations, also referred to as positively phase-correlated magnetic-density fluctuations, are primarily concentrated in two regions. One is located near the fast-mode dispersion relations (black lines), as expected for fast modes. The other appears in part of the low-frequency region at $k = [5 \times 10^{-4}, 10^{-3}] \text{ km}^{-1}$, where the inferred phase speeds are $V_{\text{ph}} = [23, 30] \text{ kms}^{-1}$, corresponding to $V_{\text{ph}}/V_A \sim 0.2$. The low phase speed suggests that these fluctuations are more likely associated with slowly propagating magnetic structures in Earth's magnetosheath, contributing to a portion of the compressible power below f_{slow} in Figs. 8(f-h). The phase-correlation analysis procedure is described in Appendix B, where we present results based on CIS-HIA proton density and WHISPER electron density that show similar behavior.

Guided by these in-phase-correlation signatures, fluctuations concentrated around the fast-mode dispersion relations are extracted as $P_{\text{BC,fast}}(f_{\text{rest}}, k) = P_{\text{BC}}(0.7f_{\text{fast}} < f_{\text{rest}} < 1.3f_{\text{fast}}, k)$, which are expected to be dominated by fast modes. Fig. 3(c) shows that $P_{\text{BC,fast}}$ is primarily distributed at $k < 8 \times 10^{-4} \text{ km}^{-1}$. As k increases, $P_{\text{BC,fast}}$ becomes progressively confined to the fast-mode dispersion relation at quasi-parallel propagation, consistent with enhanced collisionless transit-time damping of highly oblique fast modes at larger k [27, 28]. The regions where fast-mode magnetic power is enhanced coincide with regions of in-phase magnetic-density correlations (Figs. 3(c,f)), supporting the robustness of our fast-mode identification.

Figs. 3(g) and 6(a) show the $k_{\parallel} - k_{\perp}$ distribution of the fast-mode magnetic power, $P_{\text{BC,fast}}(k_{\parallel}, k_{\perp}) = \int_{0.7f_{\text{fast}}}^{1.3f_{\text{fast}}} P_{\text{BC}}(f_{\text{rest}}, k_{\parallel}, k_{\perp}) df_{\text{rest}}$. For $k < 8 \times 10^{-4} \text{ km}^{-1}$, $P_{\text{BC,fast}}$ shows only a weak dependence on the propagation angle θ in wavenumber space and does not exhibit the strong scale-dependent anisotropy characteristic of Alfvénic turbulence [20], consistent with the expected isotropic cascade of fast modes in the absence of damping at small k [23, 31]. At larger wavenumbers ($k \geq 8 \times 10^{-4} \text{ km}^{-1}$), $P_{\text{BC,fast}}$ shows an apparent in-

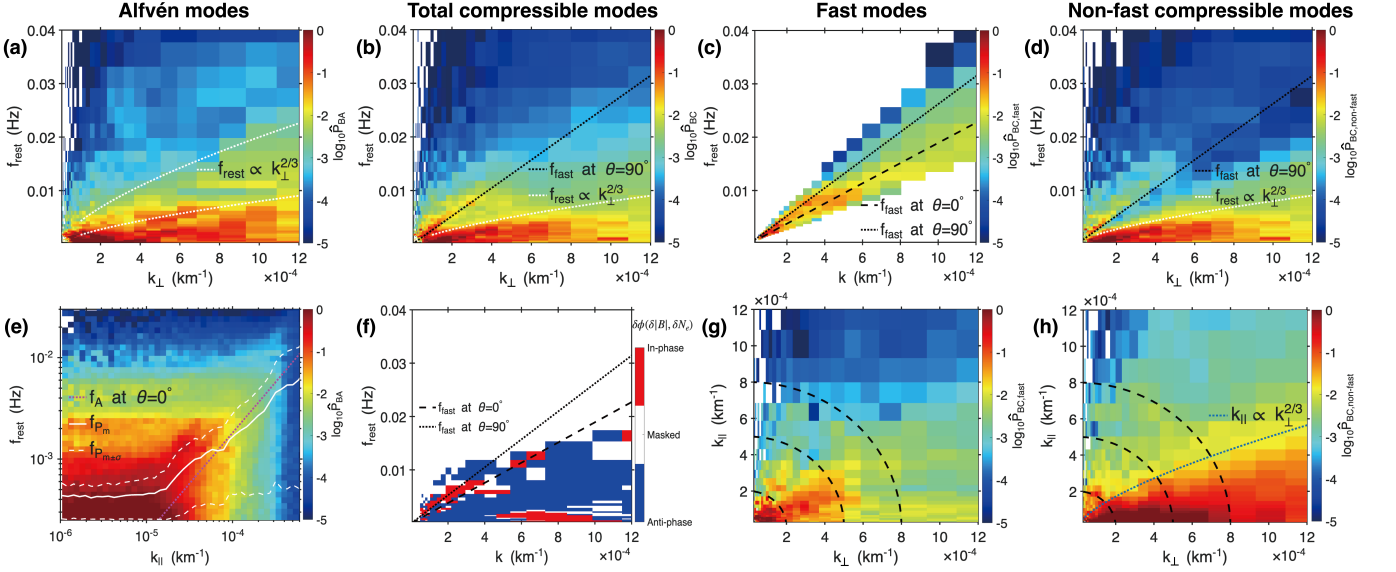


FIG. 3. Spatiotemporal power spectra of magnetic fluctuations in the plasma flow frame. (a,b,d) $f_{\text{rest}} - k_{\perp}$ distributions of Alfvénic power (\hat{P}_{BA}), total compressible power (\hat{P}_{BC}), and non-fast compressible power ($\hat{P}_{BC,\text{non-fast}}$). White dotted curves denote the scaling $f_{\text{rest}} \propto k_{\perp}^{2/3}$. Black dotted (dashed) lines denote the fast-mode dispersion relations at $\theta = 90^{\circ}$ (0°). (c) $f_{\text{rest}} - k$ distribution of fast-mode power ($\hat{P}_{BC,\text{fast}}$). (e) $f_{\text{rest}} - k_{\parallel}$ distribution of \hat{P}_{BA} . Pink dotted line denotes the Alfvén-mode dispersion relation at $\theta = 0^{\circ}$. White solid and dashed curves indicate the frequency of the mean power spectrum (f_{P_m}) and the corresponding $\pm\sigma$ confidence intervals ($f_{P_m \pm \sigma}$), where σ is the standard deviation of the power. (f) Phase correlation between fluctuating magnetic field strength ($\delta|\mathbf{B}|$) and PEACE electron density ($\delta\tilde{N}_e$), measured by Cluster-2. In-phase (anti-phase) regions correspond to phase differences within $\pm 80^{\circ}$ around 0° (180°), leaving a narrow transition region. (g,h) $k_{\parallel} - k_{\perp}$ distributions of $\hat{P}_{BC,\text{fast}}$ and $\hat{P}_{BC,\text{non-fast}}$. Blue dotted curve denotes the scaling $k_{\perp} \propto k_{\parallel}^{2/3}$. Black dashed curves denote isotropic contours at $k = 2 \times 10^{-4}$, 5×10^{-4} , and 8×10^{-4} km^{-1} . Panels with the same format are normalized by the same factor, and values smaller than 10^{-6} are set to NaN. The data are binned into $N_f \times N_{k_{\parallel}} \times N_{k_{\perp}} = 50 \times 50 \times 50$ with a threshold angle $\eta \leq 10^{\circ}$.

crease in anisotropy, likely due to contamination from anti-phase magnetic-density fluctuations. As the magnetic-density phase correlation becomes increasingly unstable (white-marked regions in Fig. 3(f)), fast-mode signatures cannot be reliably identified at these scales and are excluded from further analysis.

The remaining compressible magnetic fluctuations are collectively classified as non-fast compressible modes, defined as $P_{BC,\text{non-fast}} = P_{BC} - P_{BC,\text{fast}}$, which occupy most of the spatiotemporal space. These fluctuations exhibit nearly anti-phase magnetic-density correlations (Fig. 3(f)), in agreement with the negative phase correlation characteristic of slow and magnetic-mirror modes. As shown in Fig. 3(d), $P_{BC,\text{non-fast}}$ is concentrated at ultra-low frequencies ($f_{\text{rest}} < 5 \times 10^{-3}$ Hz) and is preferentially elongated toward higher k_{\perp} compared to the fast-mode component. This behavior agrees with theoretical expectations that slow modes dominate the low-frequency portion of the compressible spectrum [16]. Furthermore, $P_{BC,\text{non-fast}}$ follows the anisotropic scaling $k_{\parallel} \propto k_{\perp}^{2/3}$ (Fig. 3(h)), characteristic of the scale-dependent cascade of slow modes [12, 31]. Taken together, these results indicate that the non-fast compressible modes are predominantly associated with slow modes.

We note that this procedure does not completely remove all fast-mode contributions from the compressible fluctuations. This is partly because a small fraction of in-phase magnetic-density fluctuations at ultra-low frequencies, which do not follow the fast-mode dispersion relation (Figs. 3(d,f)), are included in the non-fast compressible component, and partly because the nonlinear frequency broadening of fast modes is wavenumber dependent (Fig. 6). Nevertheless, the spatiotemporal characteristics and anisotropies of $P_{BC,\text{fast}}$ and $P_{BC,\text{non-fast}}$ are consistent with the theoretical expectations for fast and slow modes, respectively, indicating that this approach provides an effective, though not exact, separation of fast-mode fluctuations from the compressible components and captures their essential dynamical behaviors.

C. Nonlinear frequency broadening of three MHD eigenmodes

To further examine nonlinear frequency broadening of MHD eigenmodes, Figs. 4, 6, and 7 present one-dimensional (1D) power spectral densities of magnetic fluctuations in the plasma flow frame at selected $(k_{\parallel}, k_{\perp})$.

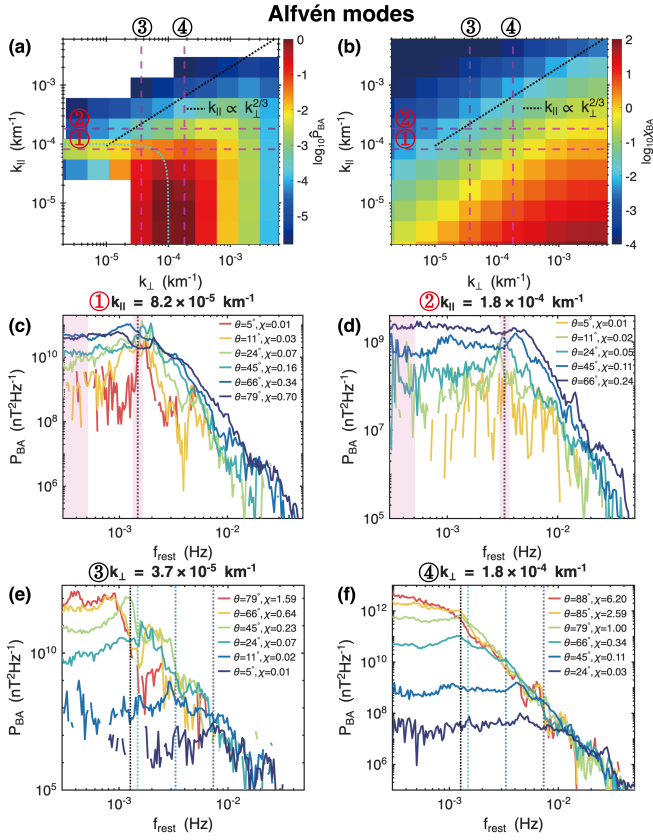


FIG. 4. Alfvénic magnetic power at selected $(k_{\parallel}, k_{\perp})$ in the plasma flow frame. (a) $k_{\parallel} - k_{\perp}$ distribution of \hat{P}_{BA} , where $\hat{P}_{BA} = P_{BA}/P_{BA,\max}$ is normalized by the maximum over all $(k_{\parallel}, k_{\perp})$ bins. Blue contour marks isotropy at $k = 10^{-4} \text{ km}^{-1}$. Black dotted lines denote the scaling $k_{\parallel} \propto k_{\perp}^{2/3}$. (b) $k_{\parallel} - k_{\perp}$ distribution of the Alfvénic nonlinearity parameter χ_{BA} . (c,d) $P_{BA}(f_{\text{rest}})$ at fixed k_{\parallel} , with color indicating k_{\perp} . The propagation angle $\theta = \arctan(k_{\perp}/k_{\parallel})$. Dotted lines indicate Alfvén frequencies f_A calculated with $k_{\parallel} = 8.2 \times 10^{-5}$ and $1.8 \times 10^{-4} \text{ km}^{-1}$. Pink-shaded regions indicate the quasi-zero-frequency power $P_{BA}(\mathbf{k}, f_{\text{rest}} \sim f_{\min}) = \frac{\int_{f_{\min}}^{5 \times 10^{-4} \text{ Hz}} P_{BA}(\mathbf{k}, f_{\text{rest}}) df_{\text{rest}}}{5 \times 10^{-4} \text{ Hz} - f_{\min}}$ and Alfvén-wave-like power $P_{BA}(\mathbf{k}, f_{\text{rest}} \sim f_A) = \frac{\int_{0.9 f_A}^{1.1 f_A} P_{BA}(\mathbf{k}, f_{\text{rest}}) df_{\text{rest}}}{0.2 f_A}$. (e,f) $P_{BA}(f_{\text{rest}})$ at fixed k_{\perp} , with color indicating k_{\parallel} . Colored dotted lines show the corresponding f_A , and black dotted lines indicate f_{A0} from $k_{\parallel,0} \sim 7 \times 10^{-5} \text{ km}^{-1}$ (Fig. 3(b) of Zhao et al. [13]). The data are binned into $N_f \times N_{k_{\parallel}} \times N_{k_{\perp}} = 200 \times 12 \times 12$ with $\eta \leq 30^\circ$ to improve statistical robustness.

1. Alfvén modes

Fig. 4(b) shows the Alfvénic nonlinearity parameter, defined as $\chi_{BA}(k_{\parallel}, k_{\perp}) = k_{\perp} \delta B_A / (k_{\parallel} B_0)$, where the Alfvénic magnetic energy density is calculated as $\delta B_A^2(k_{\parallel}, k_{\perp}) = \int_0^\infty \int_{k_{\parallel}} \int_{k_{\perp}} P_{BA}(f_{\text{rest}}, k_{\parallel}, k_{\perp}) df_{\text{rest}} dk_{\parallel} dk_{\perp}$. The parameter χ_{BA} increases either with increasing k_{\perp} or decreasing k_{\parallel} , reflecting progressively stronger nonlinear

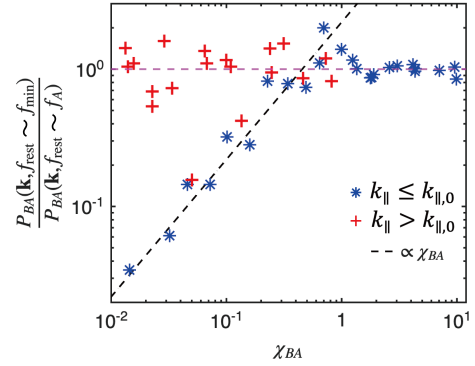


FIG. 5. Dependence of $\frac{P_{BA}(\mathbf{k}, f_{\text{rest}} \sim f_{\min})}{P_{BA}(\mathbf{k}, f_{\text{rest}} \sim f_A)}$ on the Alfvénic nonlinearity parameter χ_{BA} . The quasi-zero-frequency power $P_{BA}(\mathbf{k}, f_{\text{rest}} \sim f_{\min})$ and Alfvén-wave-like power $P_{BA}(\mathbf{k}, f_{\text{rest}} \sim f_A)$ are indicated by the pink-shaded regions in Figs. 4(c,d). The minimum frequency is $f_{\min} = 4/t_{\text{win}}$. Points with $k_{\parallel} \leq k_{\parallel,0}$ ($k_{\parallel} > k_{\parallel,0}$) are marked by asterisks (pluses), respectively. Pink horizontal line indicates $\frac{P_{BA}(\mathbf{k}, f_{\text{rest}} \sim f_{\min})}{P_{BA}(\mathbf{k}, f_{\text{rest}} \sim f_A)} = 1$, and the black dashed line indicates $\frac{P_{BA}(\mathbf{k}, f_{\text{rest}} \sim f_{\min})}{P_{BA}(\mathbf{k}, f_{\text{rest}} \sim f_A)} \propto \chi_{BA}$. Only data with $\chi_{BA} > 10^{-2}$ are included to reduce uncertainties.

interactions.

Figs. 4(c-f) show the Alfvénic magnetic power spectra $P_{BA}(f_{\text{rest}})$ at selected $(k_{\parallel}, k_{\perp})$ along four representative cuts. At $\chi_{BA} \ll 1$, the spectra exhibit pronounced peaks near the Alfvén frequency f_A , indicative of weakly nonlinear, wave-like behavior. As χ_{BA} increases, nonlinear frequency broadening becomes increasingly significant: the spectra evolve from narrow wave-like peaks to frequency-broadened distributions characterized by a plateau below f_A and a power-law decay at higher frequencies. This evolution is consistent with the weak-to-strong transition in Alfvénic turbulence [13].

Based on the analysis of Zhao et al. [13] for the same interval, at turbulence perpendicular scales larger than the transition scale ($k_{\perp} < k_{\text{tran}} \sim 5 \times 10^{-5} \text{ km}^{-1}$), the turbulent energy is primarily concentrated around a characteristic parallel wavenumber $k_{\parallel,0} = 7 \times 10^{-5} \text{ km}^{-1}$ (Fig. 4(a)). As k_{\perp} increases beyond this transition scale, P_{BA} follows the anisotropic scaling $k_{\parallel} \propto k_{\perp}^{2/3}$, indicating a transition to the strong-turbulence regime [13]. We therefore adopt $k_{\parallel,0}$ as a critical threshold to quantitatively examine how Alfvénic frequency broadening depends on the Alfvénic nonlinearity parameters χ_{BA} (Fig. 5). The strength of nonlinear frequency broadening is quantified by the power ratio $\frac{P_{BA}(\mathbf{k}, f_{\text{rest}} \sim f_{\min})}{P_{BA}(\mathbf{k}, f_{\text{rest}} \sim f_A)}$, where smaller values indicate more wave-like (i.e., less broadband) fluctuations.

Fig. 5 reveals two distinct tendencies. (1) For $k_{\parallel} \leq k_{\parallel,0}$, P_{BA} depends strongly on k_{\perp} but only weakly on k_{\parallel} (Fig. 4(a)), indicating a predominantly perpendicular cascade. In this regime, most fluctuations exhibit a quasi-2D structure with $k_{\parallel} \ll k_{\perp}$. The fluctuations reside in a mixed weak-strong regime, with a substantial

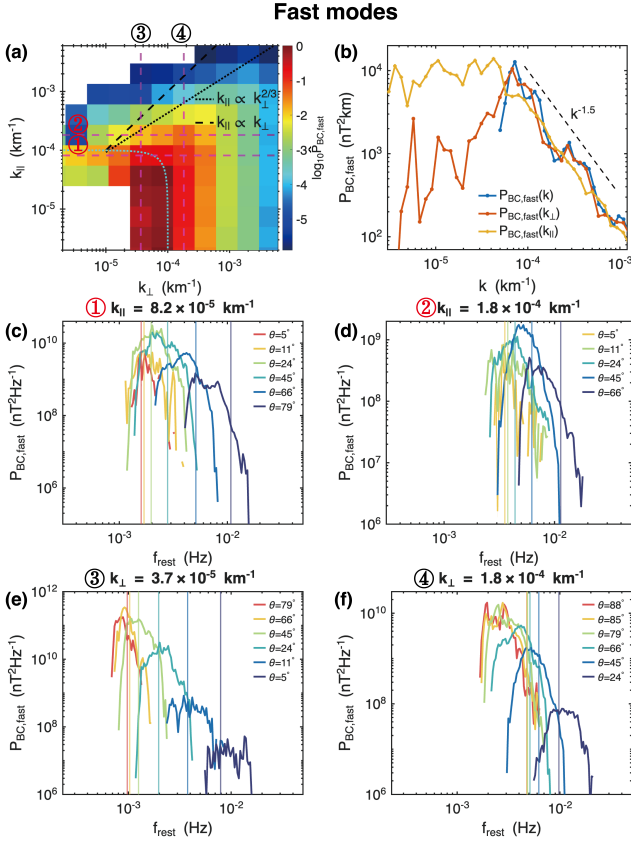


FIG. 6. Fast-mode magnetic power at selected $(k_{\parallel}, k_{\perp})$ in the plasma flow frame. (a) $k_{\parallel} - k_{\perp}$ distribution of $\hat{P}_{BC,fast}$, where $\hat{P}_{BC,fast} = P_{BC,fast}/P_{BC,fast,max}$ is normalized by the maximum over all $(k_{\parallel}, k_{\perp})$ bins. Blue contour marks isotropy at $k = 10^{-4} \text{ km}^{-1}$. Black dotted (dashed) lines denote the scaling $k_{\parallel} \propto k_{\perp}^{2/3}$ ($k_{\parallel} \propto k_{\perp}$), respectively. (b) 1D magnetic energy density of fast modes. (c,d) $\hat{P}_{BC,fast}(f_{rest})$ at fixed k_{\parallel} , with color indicating k_{\perp} . (e,f) $P_{BC,fast}(f_{rest})$ at fixed k_{\perp} , with color indicating k_{\parallel} . (c-f) Solid lines represent the fast-mode frequency f_{fast} , with lines of the same color corresponding to the same k_{\perp} or k_{\parallel} . The data are binned into $N_f \times N_{k_{\parallel}} \times N_{k_{\perp}} = 200 \times 12 \times 12$ with $\eta \leq 30^\circ$ to improve statistical robustness.

contribution from both wave-like components and slowly propagating fluctuations (Fig. 4). The power ratio increases proportionally with χ_{BA} up to $\chi_{BA} \sim 1$, where it approaches unity; for $\chi_{BA} > 1$, the ratio saturates and remains approximately equal to 1 (Fig. 5). This behavior indicates that, as nonlinearity increases, the spectra evolve from wave-like peaks to frequency-broadened distributions, reflecting the transition from weak nonlinear interactions to the strong-turbulence regime, consistent with observations [13]. (2) For $k_{\parallel} > k_{\parallel,0}$, the cascade proceeds toward higher k_{\parallel} and inevitably enters the strong-turbulence regime with a fully three-dimensional cascade. The power ratio remains close to unity (pink horizontal line), indicating the absence of a distinct wave-like spectral peak regardless of the value of χ_{BA} .

2. Fast modes

We derive 1D energy spectra of fast modes by integrating the higher-wavenumber-resolution dataset in Fig. 3(g). As shown in Fig. 6(b), the resulting spectra exhibit nearly identical power-law scalings: $P_{BC,fast}(k) \propto k^{-1.55}$, $P_{BC,fast}(k_{\perp}) \propto k_{\perp}^{-1.57}$, and $P_{BC,fast}(k_{\parallel}) \propto k_{\parallel}^{-1.52}$, fitted over the range $[8 \times 10^{-5}, 10^{-3}] \text{ km}^{-1}$. The close agreement among these spectral slopes further indicates an approximately isotropic distribution of the fast-mode energy density at these wavenumbers. The slightly steeper perpendicular spectrum $P_{BC,fast}(k_{\perp})$ relative to the parallel one $P_{BC,fast}(k_{\parallel})$ may be attributed to collisionless transit-time damping, which preferentially suppresses highly oblique fast modes [27]. This interpretation is consistent with the depletion of magnetic power near the $\theta = 90^\circ$ branch of fast-mode dispersion relations in Fig. 3(c).

Figs. 6(c-f) show the fast-mode magnetic power spectra $P_{BC,fast}(f_{rest})$ at selected $(k_{\parallel}, k_{\perp})$ along four representative cuts. Most spectra exhibit pronounced peaks near the corresponding fast-mode frequencies f_{fast} , without the low-frequency plateau or high-frequency power-law tails characteristic of strongly nonlinear fluctuations. This behavior indicates that fast modes remain predominantly wave-like, experiencing only modest nonlinear frequency broadening, consistent with simulation expectations [16]. Consequently, fast-mode fluctuations remain in the weak-turbulence regime and do not transition to strong turbulence as the cascade proceeds to smaller scales.

As θ approaches 90° , $P_{BC,fast}$ exhibits enhanced power at frequencies well below f_{fast} (Figs. 6(c,f)), likely due to contamination by anti-phase magnetic-density fluctuations near the fast-mode dispersion relations (Fig. 3(f)) and the limited cascade of fast modes toward higher k_{\perp} (Figs. 3(f,g)). Nevertheless, this effect does not alter the main conclusion that fast modes remain predominantly wave-like and persist in the weak-turbulence regime over the observed wavenumber range.

3. Non-fast compressible modes

As discussed above, non-fast compressible fluctuations are predominantly dominated by slow modes, which are expected to be passively cascaded by Alfvénic turbulence [24–26]. By analogy with the Alfvénic nonlinearity parameter χ_{BA} , we define the non-fast compressible nonlinearity parameter as $\chi_{BC,non-fast}(k_{\parallel}, k_{\perp}) = k_{\perp} \delta B_{BC,non-fast} / (k_{\parallel} B_0)$, where the non-fast compressible energy density is given by $\delta B_{BC,non-fast}^2(k_{\parallel}, k_{\perp}) = \int_0^\infty \int_{k_{\parallel}}^\infty \int_{k_{\perp}}^\infty P_{BC,non-fast}(f_{rest}, k_{\parallel}, k_{\perp}) df_{rest} dk_{\parallel} dk_{\perp}$, as shown in Fig. 7(b). The parameter $\chi_{BC,non-fast}$ increases either with increasing k_{\perp} or decreasing k_{\parallel} , reflecting progressively stronger nonlinear interactions.

Figs. 7(c-f) show the non-fast compressible magnetic

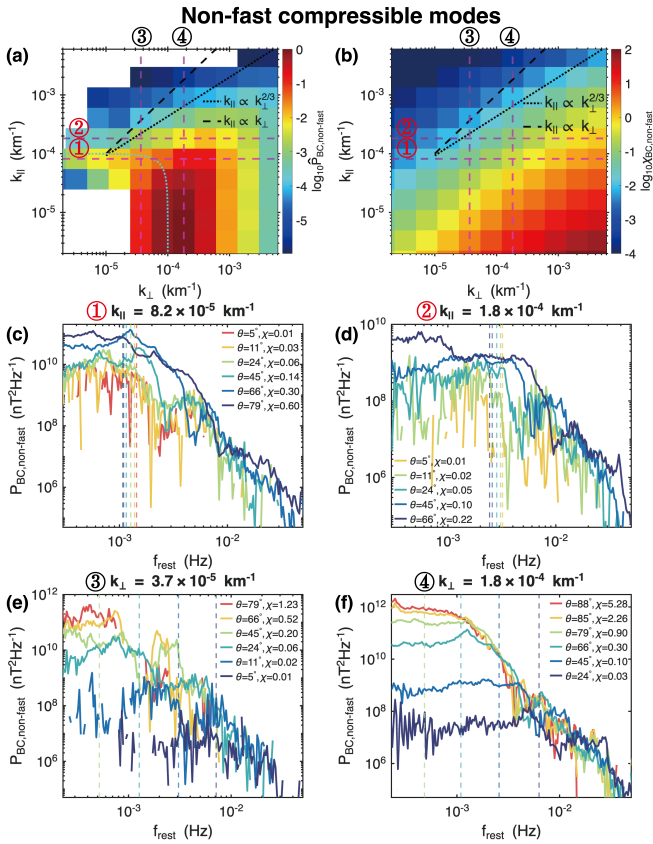


FIG. 7. Non-fast compressible magnetic power at selected $(k_{\parallel}, k_{\perp})$ in the plasma flow frame. (a) $k_{\parallel} - k_{\perp}$ distribution of $\hat{P}_{BC,non-fast}$, where $\hat{P}_{BC,non-fast} = P_{BC,non-fast}/P_{BC,non-fast,max}$ is normalized by the maximum over all $(k_{\parallel}, k_{\perp})$ bins. Blue contour marks isotropy at $k = 10^{-4} \text{ km}^{-1}$. Black dotted (dashed) lines denote the scaling $k_{\parallel} \propto k_{\perp}^{2/3}$ ($k_{\parallel} \propto k_{\perp}$), respectively. (b) $k_{\parallel} - k_{\perp}$ distribution of the non-fast nonlinearity parameter $(\chi_{BC,non-fast})$. (c,d) $P_{BC,non-fast}(f_{rest})$ at fixed k_{\parallel} , with color indicating k_{\perp} . (e,f) $P_{BC,non-fast}(f_{rest})$ at fixed k_{\perp} , with color indicating k_{\parallel} . (c-f) Dashed lines represent the slow-mode frequency f_{slow} , with lines of the same color corresponding to the same k_{\perp} or k_{\parallel} . The data are binned into $N_f \times N_{k_{\parallel}} \times N_{k_{\perp}} = 200 \times 12 \times 12$ with $\eta \leq 30^\circ$ to improve statistical robustness.

power spectra $P_{BC,non-fast}(f_{rest})$ at selected $(k_{\parallel}, k_{\perp})$ along four representative cuts. Similar to Alfvénic fluctuations, for $\chi_{BC,non-fast} \ll 1$, most spectral peaks are concentrated near the slow-mode frequency f_{slow} (Figs. 7(d,e)), confirming that these fluctuations are predominantly wave-like and primarily associated with slow modes. As $\chi_{BC,non-fast}$ increases, $P_{BC,non-fast}$ evolves from wave-like peaks to frequency-broadened spectra characterized by a plateau below f_{slow} and a power-law decay at higher frequencies (Figs. 7(e,f)). This evolution provides evidence that slow modes undergo a weak-to-strong turbulence transition, similar to that observed in Alfvénic turbulence [13].

Overall, the nonlinear frequency broadening of $P_{BC,non-fast}(f_{rest})$ is broadly consistent with that of

Alfvénic fluctuations, with the main difference being broader and less distinct spectral peaks near f_{slow} (Figs. 4 and 7). This difference may arise not only from the intrinsically stronger nonlinearity of slow modes [16], but also from additional non-slow-mode contributions that enhance the broadband character of the spectrum, such as in-phase magnetic-density fluctuations at ultra-low frequencies (Fig. 3(f)).

IV. ASTROPHYSICAL AND SPACE IMPLICATIONS

By quantifying how distinct wave modes distribute their energy across spatial scales and frequencies, this study reveals the spatiotemporal properties of compressible turbulence. Our results extend the weak-to-strong turbulence transition known for incompressible Alfvénic turbulence to the compressible regime: slow modes exhibit a weak-to-strong transition, evolving from wave-like peaks to frequency-broadened spectra as nonlinearity increases, whereas fast modes remain weakly turbulent with narrow peaks near their eigenfrequencies (Figs. 6 and 7). These findings provide important observational constraints and lay the foundation for a general framework describing multi-scale, multi-mode dynamics in compressible turbulence theory.

Additionally, ultra-low-frequency (ULF) waves in the solar wind and Earth’s foreshock are important drivers of magnetospheric Pc4-5 waves (e.g., [46]; see also the review by Menk [47]). However, how they propagate through the Earth’s magnetosheath into the magnetosphere remains unclear. Our results suggest that fast-mode components can remain largely wave-like during transmission across the magnetosheath, owing to weak nonlinear frequency broadening and a nearly isotropic cascade (Fig. 6). In contrast, Alfvén, and slow modes undergo rapid nonlinear decorrelation and structuralization, progressively losing coherent wave characteristics (Figs. 4 and 7). Consequently, fast modes could efficiently reach the magnetopause and drive magnetospheric ULF waves via compressional coupling and field-line resonances, whereas the other modes may be far less effective in this role.

Furthermore, turbulent reconnection occurs within a pre-existing current sheet embedded in a turbulent environment, where the wandering of magnetic field lines associated with turbulent fluctuations plays a dominant role [48, 49]. Such current sheets can naturally emerge as coherent structures formed by nonlinear interactions in turbulent fluctuations and their anisotropic cascades [50, 51]. Our results show that Alfvén and slow modes dominate turbulence in Earth’s magnetosheath. Their anisotropic cascades generate anisotropic sheet-like structures, linking turbulent reconnection to the nonlinear evolution of Alfvénic turbulence. In contrast, fast modes undergo a more isotropic cascade that is less conducive to the formation of thin current sheets. These

findings establish a mode-resolved connection between the mode composition of turbulence and reconnection physics.

V. CONCLUSION

In this study, we advance the polarization-based mode-decomposition method of Zhao et al. [33], augmented by incorporating the phase correlation between fluctuations in magnetic field strength $\delta|\tilde{\mathbf{B}}|$ and plasma density $\delta\tilde{N}$. Using this approach, we obtain spatiotemporal power spectra of the three MHD eigenmodes and present the first quantitative assessment of frequency broadening due to nonlinear interactions. Our main findings are summarized below.

(1) The nonlinear frequency broadening of Alfvén modes exhibits two distinct tendencies at $k_{\parallel} \leq k_{\parallel,0}$ and $k_{\parallel} > k_{\parallel,0}$. (i) For $k_{\parallel} \leq k_{\parallel,0}$, Alfvén modes evolve from wave-like peaks to frequency-broadened spectra as nonlinearity increases, developing plateaus below f_A and power-law tails at higher frequencies, consistent with observations [13]. (ii) In contrast, for $k_{\parallel} > k_{\parallel,0}$, the fluctuations inevitably enter the strong-turbulence regime with a fully three-dimensional cascade, and Alfvénic spectra exhibit no distinct wave-like spectral peak regardless of the value of χ_{BA} (Figs. 4 and 5).

(2) Compressible fluctuations exhibit two distinct components: one follows the fast-mode dispersion relation with in-phase magnetic–density correlations, consistent with fast modes; the other (referred to as non-fast compressible modes) follows the scaling $f_{\text{rest}} \propto k_{\perp}^{2/3}$ with anti-phase magnetic–density correlations, consistent with slow modes (Fig. 3).

(3) Fast-mode spectra retain narrow peaks near f_{fast} , indicating weak nonlinearity across the inertial range (Fig. 6). In contrast, non-fast compressible modes, dominated by slow modes, evolve from wave-like peaks to frequency-broadened spectra as nonlinearity increases (Fig. 7), indicating that slow modes undergo a transition from weak to strong turbulence.

(4) At large scales ($k_{\parallel} < 10^{-5} \text{ km}^{-1}$), both P_{BA} and P_{BC} exhibit nearly constant low-frequency fluctuations around $f_{\text{rest}} \sim 5 \times 10^{-4} \text{ Hz}$ with $k_{\parallel} \ll k_{\perp}$ (Figs. 3(e) and 8(g)), indicating that both Alfvénic and compressible fluctuations contribute significantly to low-frequency, large-scale quasi-2D magnetic structures.

These results provide a comprehensive observational characterization of turbulence across mode composition, spatiotemporal space, and both weak- and strong-turbulence regimes, with broad implications for turbulence-mediated processes, including particle transport and acceleration [27, 52–54], turbulent magnetic reconnection [17, 55, 56], heating of solar and stellar winds [29, 57], and star formation [58, 59]. Given the representative plasma conditions of this event, the spatiotemporal properties of compressible MHD turbulence identified here are likely to be generic across a broad range

of plasma environments, from the solar corona and interplanetary space to the interstellar medium.

ACKNOWLEDGMENTS

We acknowledge the members of the Cluster spacecraft team and NASA’s Coordinated Data Analysis Web. The Cluster data are available at <https://cdaweb.gsfc.nasa.gov>. Data analysis was performed using the IRFU-MATLAB analysis package [60] available at <https://github.com/irfu/irfu-matlab>. We acknowledge the use of ChatGPT to improve English grammar and sentence structure. C.H. is supported by the Alexander von Humboldt Foundation.

Appendix A: Spatiotemporal power spectra of fluctuations

Fig. 8 shows the spatiotemporal power spectra of velocity, magnetic, and density fluctuations in the plasma flow frame. The spectra of different physical quantities within the same mode exhibit similar energy distributions, demonstrating the robustness and reliability of the mode decomposition of turbulence.

Appendix B: Method for Analyzing the Phase Correlation Between Magnetic Field Strength and Plasma Density Fluctuations

The time series of magnetic field strength and plasma density are transformed using the Morlet-wavelet transform [44], yielding Fourier-space fluctuations in GSE coordinates: $\delta|\tilde{\mathbf{B}}|(t, f_{\text{sc}})$ and $\delta\tilde{N}(t, f_{\text{sc}})$. The phase difference $\delta\tilde{\phi}(t, f_{\text{sc}})$ is defined as the phase angle of their complex cross-spectrum, calculated by multiplying $\delta|\tilde{\mathbf{B}}|$ with the complex conjugate of $\delta\tilde{N}$. The resulting phase is expressed in radians and lies within the range $(-\pi, \pi]$.

To obtain the spatiotemporal distribution of the phase relation in the plasma flow frame, we construct a set of $N_f \times N_{k_{\parallel}} \times N_{k_{\perp}} = 50 \times 50 \times 50$ bins in $(f_{\text{rest}}, k_{\parallel}, k_{\perp})$ space, applying an angle threshold of $\eta \leq 10^\circ$. For each time–frequency sample, the phase difference $\tilde{\phi}$ is represented as a unit complex vector $e^{i\tilde{\phi}}$ and accumulated with weight $w = \sqrt{P_{|\mathbf{B}}|P_N}$, where $P_{|\mathbf{B}}| = |\delta|\tilde{\mathbf{B}}||^2$ and $P_N = |\delta\tilde{N}|^2$. For each $(f_{\text{rest}}, k_{\parallel}, k_{\perp})$ bin, the weighted circular-averaged phase angle is defined as $\delta\phi = \arg\left(\frac{\sum w e^{i\tilde{\phi}}}{\sum w}\right)$, and the corresponding phase-locking value is defined as $L = \left|\frac{\sum w e^{i\tilde{\phi}}}{\sum w}\right|$, which quantifies the coherence of the phase relation within the bin. Each bin has an associated energy density. Fig. 3(f) and 9 display only those bins whose energy density ranks within the top 70% of the cumulative energy, with the additional requirement $L > 0.3$ to ensure phase stability.

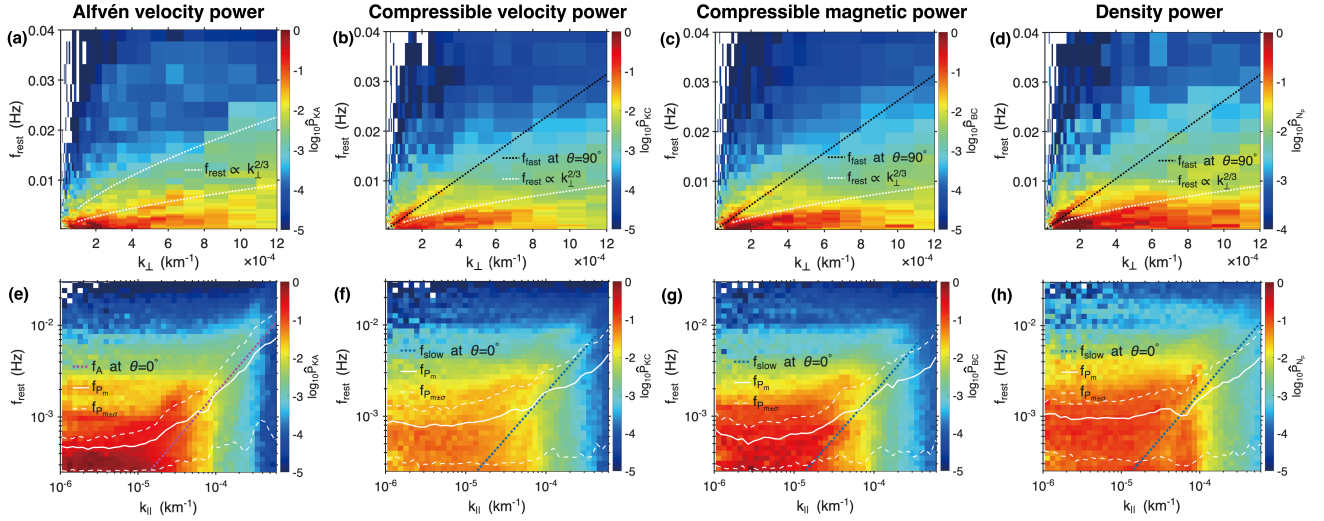


FIG. 8. Spatiotemporal power spectra of velocity and density fluctuations. (a-d) $f_{\text{rest}} - k_{\perp}$ distributions of Alfvénic velocity power (\hat{P}_{KA}), compressible velocity power (\hat{P}_{KC}), compressible magnetic power (\hat{P}_{BC}), and proton density power (\hat{P}_{N_p}). (e-h) $f_{\text{rest}} - k_{\parallel}$ distributions of \hat{P}_{KA} , \hat{P}_{KC} , \hat{P}_{BC} , and \hat{P}_{N_p} . Black dotted lines denote fast-mode dispersion relations at $\theta = 90^\circ$. Pink and blue dotted lines denote the dispersion relations of Alfvén and slow modes at $\theta = 0^\circ$, respectively. White solid curves mark the frequencies of the mean power spectrum, whereas white dashed curves indicate $\pm\sigma$ confidence intervals, where σ is the standard deviation of the power. Panels with the same format are normalized by the same factor, and normalized values smaller than 10^{-6} are set to NaN. The data are binned into $N_f \times N_{k_{\parallel}} \times N_{k_{\perp}} = 50 \times 50 \times 50$ and restricted to $\eta \leq 10^\circ$.

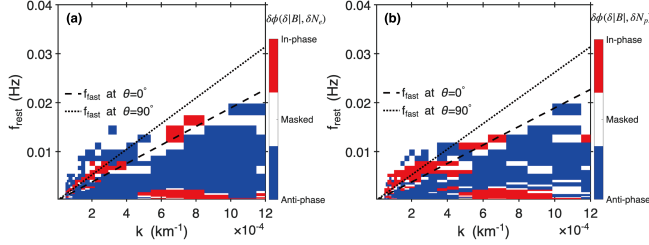


FIG. 9. Phase correlation between fluctuations in magnetic field strength and plasma density. (a) Phase correlation between $\delta|\tilde{\mathbf{B}}|$ and CIA-HIA proton density $\delta\tilde{N}_p$. (b) Phase correlation between $\delta|\tilde{\mathbf{B}}|$ and WHISPER electron density $\delta\tilde{N}_e$.

- [1] G. P. Zank and W. H. Matthaeus, Waves and turbulence in the solar wind, *J. Geophys. Res.* **97**, 17189 (1992).
- [2] J. W. Armstrong, B. J. Rickett, and S. R. Spangler, Electron Density Power Spectrum in the Local Interstellar Medium, *Astrophys. J.* **443**, 209 (1995).
- [3] A. Lazarian, A. Beresnyak, H. Yan, M. Opher, and Y. Liu, Properties and selected implications of magnetic turbulence for interstellar medium, local bubble and solar wind, *Space Sci. Rev.* **143**, 387 (2008).
- [4] R. M. Crutcher, Magnetic Fields in Molecular Clouds, *Annu. Rev. Astron. Astrophys.* **50**, 29 (2012).
- [5] G. Brunetti and A. Lazarian, Compressible turbulence in galaxy clusters: Physics and stochastic particle re-acceleration, *Mon. Not. Royal Astron. Soc.* **378**, 245 (2007).
- [6] R. Bruno and V. Carbone, The Solar Wind as a Turbulence Laboratory, *Living Rev. Sol. Phys.* **10**, 2 (2013).
- [7] H. Yan, Magnetohydrodynamic turbulence and propagation of cosmic rays: theory confronted with observations, *icrc*, 038 (2021).
- [8] A. Kolmogorov, The Local Structure of Turbulence in Incompressible Viscous Fluid for Very Large Reynolds' Numbers, *Akademiia Nauk SSSR Doklady* **30**, 301 (1941).
- [9] P. Iroshnikov, Turbulence of a Conducting Fluid in a Strong Magnetic Field, *Soviet Astronomy* **7**, 566 (1964).
- [10] A. Verdini and R. Grappin, Transition from weak to strong cascade in MHD turbulence, *Phys. Rev. Lett.* **109**, 1 (2012).
- [11] R. Meyrand, S. Galtier, and K. H. Kiyani, Direct Evidence of the Transition from Weak to Strong Magnetohydrodynamic Turbulence, *Phys. Rev. Lett.* **116**, 105002 (2016).

- (2016).
- [12] K. D. Makwana and H. Yan, Properties of Magnetohydrodynamic Modes in Compressively Driven Plasma Turbulence, *Phys. Rev. X* **10**, 031021 (2020).
- [13] S. Zhao, H. Yan, T. Z. Liu, K. H. Yuen, and H. Wang, Identification of the weak-to-strong transition in Alfvénic turbulence from space plasma, *Nat. Astron.* **8**, 725 (2024).
- [14] J. V. Hollweg, Waves and instabilities in the solar wind, *Rev. Geophys.* **13**, 263 (1975).
- [15] D. Verscharen, K. G. Klein, and B. A. Maruca, Living Rev. Sol. Phys., Living Reviews in Solar Physics **16**, 5 (2019).
- [16] K. H. Yuen, H. Li, and H. Yan, Temporal Properties of Compressible Magnetohydrodynamic Turbulence, *Astrophys. J.* **986**, 221 (2025).
- [17] A. Lazarian and E. T. Vishniac, Reconnection in a Weakly Stochastic Field, *Astrophys. J.* **517**, 700 (1999).
- [18] S. Galtier, S. V. Nazarenko, A. C. Newell, and A. Pouquet, A weak turbulence theory for incompressible magnetohydrodynamics, *J. Plasma Phys.* **63**, 447 (2000).
- [19] J. V. Shebalin, W. H. Matthaeus, and D. Montgomery, Anisotropy in MHD turbulence due to a mean magnetic field, *J. Plasma Phys.* **29**, 525 (1983).
- [20] P. Goldreich and S. Sridhar, Toward a theory of interstellar turbulence. 2: Strong alfvénic turbulence, *Astrophys. J.* **438**, 763 (1995).
- [21] Z. Gan, H. Li, X. Fu, and S. Du, On the Existence of Fast Modes in Compressible Magnetohydrodynamic Turbulence, *Astrophys. J.* **926**, 222 (2022).
- [22] S. Galtier, Weak inertial-wave turbulence theory, *Phys. Rev. E* **68**, 015301 (2003).
- [23] C. Hou, H. Yan, S. Zhao, and P. Pavaskar, Energy Cascade and Damping in Fast-mode Compressible Turbulence, *The Astrophysical Journal Letters* **992**, L28 (2025).
- [24] Y. Lithwick and P. Goldreich, Compressible Magnetohydrodynamic Turbulence in Interstellar Plasmas, *Astrophys. J.* **562**, 279 (2001).
- [25] J. Cho and A. Lazarian, Compressible magnetohydrodynamic turbulence: Mode coupling, scaling relations, anisotropy, viscosity-damped regime and astrophysical implications, *MNRAS* **345**, 325 (2003).
- [26] A. A. Schekochihin, S. C. Cowley, W. Dorland, G. W. Hammett, G. G. Howes, E. Quataert, and T. Tatsuno, Astrophysical gyrokinetics: Kinetic and fluid turbulent cascades in magnetized weakly collisional plasmas, *The Astrophysical Journal Supplement Series* **182**, 310 (2009).
- [27] H. Yan and A. Lazarian, Cosmic-Ray Scattering and Streaming in Compressible Magnetohydrodynamic Turbulence, *Astrophys. J.* **614**, 757 (2004).
- [28] V. Petrosian, H. Yan, and A. Lazarian, Damping of Magnetohydrodynamic Turbulence in Solar Flares, *Astrophys. J.* **644**, 603 (2006).
- [29] T. K. Suzuki, H. Yan, A. Lazarian, and et al., Collisionless Damping of Fast Magnetohydrodynamic Waves in Magnetorotational Winds, *Astrophys. J.* **640**, 1005 (2006).
- [30] K. Glassmeier, U. Motschmann, and R. Stein, Mode recognition of MHD wave fields at incomplete dispersion measurements, *Ann. Geophys.* **13**, 76 (1995).
- [31] J. Cho and A. Lazarian, Compressible Sub-Alfvénic MHD Turbulence in Low- β Plasmas, *Phys. Rev. Lett.* **88**, 245001 (2002).
- [32] G. P. Zank, L.-L. Zhao, L. Adhikari, M. Nakanotani, A. Pitňa, D. Telloni, and H. Che, Linear Mode Decomposition in Magnetohydrodynamics Revisited, *The Astrophysical Journal Supplement Series* **268**, 18 (2023).
- [33] S. Zhao, H. Yan, T. Z. Liu, and C. Hou, Mode Composition Shapes Magnetic Anisotropy in Solar Wind Turbulence, *Astrophys. J.* **996**, 46 (2026).
- [34] G. I. Taylor, The Spectrum of Turbulence, *Proc. R. Soc. Lond. A* **164**, 476 (1938).
- [35] A. Balogh, M. W. Dunlop, S. W. H. Cowley, and et al., The Cluster Magnetic Field Investigation, *Space Sci. Rev.* **79**, 65 (1997).
- [36] H. Rème, C. Aoustin, J. M. Bosqued, and et al., First multispacecraft ion measurements in and near the Earth's magnetosphere with the identical Cluster ion spectrometry (CIS) experiment, *Ann. Geophys.* **19**, 1303 (2001).
- [37] A. D. Johnstone, C. Alsop, S. Burge, and et al., Peace: A Plasma Electron and Current Experiment, *Space Sci. Rev.* **79**, 351 (1997).
- [38] P. M. E. Décréau, P. Fergeau, V. Krannosels'kikh, and et al., WHISPER, A Resonance Sounder and Wave Analyser: Performances and Perspectives for the Cluster Mission, *Space Sci. Rev.* **79**, 157 (1997).
- [39] S. Zhao, H. Yan, T. Z. Liu, K. H. Yuen, and M. Shi, Small-amplitude Compressible Magnetohydrodynamic Turbulence Modulated by Collisionless Damping in Earth's Magnetosheath: Observation Matches Theory, *Astrophys. J.* **962**, 89 (2024).
- [40] O. Santolík, M. Parrot, and F. Lefeuvre, Singular value decomposition methods for wave propagation analysis, *Radio Sci.* **38**, 1010 (2003).
- [41] J. Cho and E. T. Vishniac, The Anisotropy of Magnetohydrodynamic Alfvénic Turbulence, *Astrophys. J.* **539**, 273 (2000).
- [42] S. Zhao, H. Yan, T. Z. Liu, and et al., Multispacecraft Analysis of the Properties of Magnetohydrodynamic Fluctuations in Sub-Alfvénic Solar Wind Turbulence at 1 au, *Astrophys. J.* **937**, 102 (2022).
- [43] K. H. Yuen, H. Yan, and A. Lazarian, Anomalous compressible mode generation by global frame projections of pure Alfvén mode, *MNRAS* **521**, 530 (2023).
- [44] A. Grinsted, J. C. Moore, and S. Jevrejeva, Application of the cross wavelet transform and wavelet coherence to geophysical time series, *Nonlin. Processes Geophys.* **11**, 561 (2004).
- [45] J.-L. Pinçon and K.-H. Glassmeier, Multi-Spacecraft Methods of Wave Field Characterisation, *ISSI Scientific Report SR-008*, 91 (1998).
- [46] L. Turc, O. W. Roberts, D. Verscharen, A. P. Dimmock, P. Kajdič, M. Palmroth, Y. Pfau-Kempf, A. Johlander, M. Dubart, E. K. J. Kilpua, J. Soucek, K. Takahashi, N. Takahashi, M. Battarbee, and U. Ganse, Transmission of foreshock waves through Earth's bow shock, *Nature Physics* **19**, 78 (2023).
- [47] F. W. Menk, Magnetospheric ULF Waves: A Review, in *The Dynamic Magnetosphere* (Springer Netherlands, Dordrecht, 2011) pp. 223–256.
- [48] G. L. Eyink, Turbulent General Magnetic Reconnection, *Astrophysical Journal* **807**, 137 (2015).
- [49] A. Lazarian, G. Eyink, E. Vishniac, and G. Kowal, Turbulent reconnection and its implications, *Philosophical Transactions of the Royal Society A: Mathematical,*

- Physical and Engineering Sciences **373**, 20140144 (2015).
- [50] W. H. Matthaeus and S. L. Lamkin, Turbulent magnetic reconnection, *The Physics of Fluids* **29**, 2513 (1986).
- [51] S. Boldyrev, Spectrum of magnetohydrodynamic turbulence, *Phys. Rev. Lett.* **96**, 115002 (2006).
- [52] R. Schlickeiser, *Theoretical Physics and Astrophysics*, Astronomy and Astrophysics Library (2002) pp. 343–387.
- [53] H. Yan, A. Lazarian, and V. Petrosian, Particle acceleration by fast modes in solar flares, *The Astrophysical Journal* **684**, 1461 (2008).
- [54] S. Maiti, K. Makwana, H. Zhang, and H. Yan, Cosmic-ray Transport in Magnetohydrodynamic Turbulence, *Astrophys. J.* **926**, 94 (2022).
- [55] W. H. Matthaeus, M. L. Goldstein, and S. R. Lantz, The alpha dynamo parameter and measurability of helicities in magnetohydrodynamic turbulence, *Phys. Fluids* **29**, 1504 (1986).
- [56] W. Daughton, V. Roytershteyn, H. Karimabadi, L. Yin, B. J. Albright, B. Bergen, and K. J. Bowers, Role of electron physics in the development of turbulent magnetic reconnection in collisionless plasmas, *Nature Physics* **7**, 539 (2011).
- [57] W. H. Matthaeus, G. P. Zank, C. W. Smith, and S. Oughton, Turbulence, spatial transport, and heating of the solar wind, *Phys. Rev. Lett.* **82**, 3444 (1999).
- [58] C. J. Lada, M. Lombardi, and J. F. Alves, ON THE STAR FORMATION RATES IN MOLECULAR CLOUDS, *Astrophys. J.* **724**, 687 (2010).
- [59] P. Padoan, T. Haugbølle, Å. Nordlund, and S. Frimann, Supernova Driving. IV. The Star-formation Rate of Molecular Clouds, *Astrophys. J.* **840**, 48 (2017).
- [60] Y. Khotyaintsev and et al, IRFU-Matlab (2024).